Available online at www.sciencedirect.com

SciVerse ScienceDirect

Proceedings of the Combustion Institute 34 (2013) 3135–3143

Proceedings of the Combustion Institute

www.elsevier.com/locate/proci

Effects of hydrogen on the thermo-acoustics coupling mechanisms of low-swirl injector flames in a model gas turbine combustor

D.W. Davis [a], P.L. Therkelsen [b], D. Littlejohn [b], R.K. Cheng [b,*]

[a] United Technologies Research Center, East Hartford, CT, USA
[b] Lawrence Berkeley National Laboratory, MS 70-108B, 1 Cyclotron Rd., Berkeley, CA 94720, USA

Available online 27 June 2012

Abstract

The effects of hydrogen on the dynamic response of self-excited oscillations in a model low-swirl injector (LSI) gas turbine combustor have been studied by high-speed imaging of flame light emissions and OH^* chemiluminescence on two thermoacoustically coupled unsteady flames burning CH_4 (113 kW) and a fuel blend of $0.9H_2/0.1CH_4$ (74 kW). The two flames have different shapes. The CH_4 flame is lifted and bowl-shaped and the $0.9H_2/0.1CH4$ flame is attached and M-shaped. From phase-resolved PIV, the dominant unsteady flow structures of both flames are ring vortices shed from the LSI exit rim. The vortices of the CH_4 flame burn intermittently and those in the $0.9H_2/0.1CH_4$ flame burn consistently. Proper orthogonal decomposition analysis of OH^* and calculation of Rayleigh indices show different flame structures are responsible for generating flame oscillations and acoustic coupling. CH_4 flame oscillations are associated with flame folding near the standing ring vortex below the trailing edge of the lifted flame, intermittent burning of the shear layer, and irregular acoustic driving. The $0.9H_2/0.1CH_4$ flame has regular and stronger forcing. A key contributor to the $0.9H_2/0.1CH_4$ flame driving is merging of the central flat flame with the reacting rolled-up vortices, resulting in an instantaneous narrow band of localized high heat release density that is in phase with the pressure oscillation. Cyclic variations in the flow of the reactants also contribute to non-linear effects. High reactivity of H_2 generates a situation where the geometry of the attached shear layer flame and central disk-shaped flame creates a very favorable situation for exciting higher-pressure oscillations at a lower total heat release than CH_4 flames. To control combustion oscillations in a fuel-flexible LSI gas turbine combustor, the mitigation of flame attachment and/or formation of the outer shear layer would be necessary.

Keywords: Gas turbines; Combustion oscillations; Hydrogen; Lean premixed; Swirl

1. Introduction

Recent advances in lean premixed combustion technologies have been shown to be highly effective in reducing NO_x emissions from gas turbines of all sizes. However, mitigating the propen-

* Corresponding author. Fax: +1 510 486 7303.
E-mail address: RKCheng@lbl.gov (R.K. Cheng).

1540-7489/$ - see front matter © 2012 United Technologies Corporation and The Combustion Institute. Published by Elsevier Inc. All rights reserved.
http://dx.doi.org/10.1016/j.proci.2012.05.050

sities of lean premixed combustors to incite thermo-acoustic oscillations remains a significant challenge. Coupling of the combustion process (i.e. a flame) and the unsteady fluid mechanics can result in oscillatory fluid motion, often termed combustion instability. The energy for the oscillatory fluid motion is supplied by the dynamic heat release of the combustion process [1–3]. Combustion instability in many systems involves the interaction of a large scale fluid structure such as a vortex with a flame [2]. This interaction generates periodic variation of the flame geometry, altering the intensity and location of the heat release. In gas turbines for power generation, efforts in reducing combustion oscillation are exacerbated when fuel-flexible operation is desired. Due to variations in size, position and heat release density, flames burning low-heating value fuels from renewable sources, syngases from coal gasification, and high-hydrogen content (HHC) fuels will incite different combustor responses than flames burning natural gas, thus opening potential for additional combustion instability modes.

Much of the research on combustion oscillations focuses on flames stabilized in highly swirling flows, typical of those in contemporary gas turbines. In this configuration, vortices in the central recirculation zone and in the inner and outer shear layers (ISL and OSL) of the swirl jet can be sources of combustion oscillations. Experiments on forced [4,5] and self-excited [6,7] unstable swirling flames show them to assume vastly different flame structures and oscillation characteristics. Recent studies also show the use of different fuels altering the overall flame shape and thus the oscillations responses [8,9].

The present study focuses on investigating the oscillations characteristics of a low-swirl injector (LSI) which utilizes a different flame stabilization mechanism than the high-swirl approach [10,11]. The LSI generates a central non-recirculating divergence flow that allows the premixed flame to propagate freely. Laboratory studies and rig-tests show the LSI to be a viable technology for ultra-low emissions fuel-flexible gas turbine [12–14]. When burning CH_4, the LSI flame is detached and assumes a bowl shape (Fig. 1, left). The use of HHC fuels such as a blend of $0.9H_2/0.1CH_4$ causes the flame to attach to the rim and changes the flame to M-shape (Fig. 1, right) [13]. This also implies a change in the stabilization mechanism and the oscillation characteristics. Being a recent development, knowledge of LSI flame instability is limited to a few laboratory studies [15–18] and the fuel effects on flame stability and oscillations characteristics remain largely unexplored.

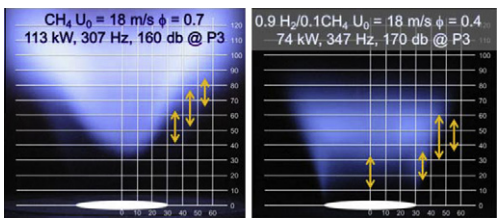

Fig. 1. Photographs of the two flames and their conditions. Orange arrows mark the locations where oscillations were reported in Ref. [19] (For interpretation of the references to color in this figure legend, the reader is referred to the web version of this article.).

2. Background and objective

Previously, Therkelsen et al. [19] studied unsteady behaviors of LSI flames burning CH_4 and $0.9H_2/0.1CH_4$ in a model gas turbine combustor. The diagnostics included pressure sensors, laser schlieren flame motion detection, and phase-resolved particle image velocimetry (PIV). Of the 48 flames investigated by varying velocity, U_0, equivalence ratio, ϕ, and chamber length, six were found to be thermoacoustically coupled, generating pressure fluctuations close to the primary acoustic frequencies near the first longitudinal (1 L) mode of the system. However, acoustic pressure levels, and periodic flowfield behaviors were different for the two fuels. Two baseline flames were investigated in details (Fig. 1). From PIV, the dominant unsteady flowfield structures in both flames were the traveling non-helical ring vortices in the OSL shed from the rim of the LSI. By estimating the convection speed of the ring vortices, a delay time, τ, between vortex formation and flame response was calculated and used in a linear stability analysis by n–τ type model. The vortices are shown to be the basic driving mechanism of the unstable CH_4 flame. But for the $0.9H_2/0.1CH_4$, due to flame attachment, flame and velocity oscillations also occur in the central region where large-scale vortices are absent; the n–τ model is not appropriate. Therefore, the driving mechanism of the unstable $0.9H_2/0.1CH_4$ flame is unclear. For both flames, how the oscillating flame structures coupled with the traveling vortex structures to incite pressure fluctuations remains unresolved.

Our objective is to characterize the flame/vortex interaction processes of the two self-excited unstable flames and the coupling to the heat release oscillation by using high-speed imaging of broadband flame light emission and OH (OH^*) chemiluminescence. These line-of-sight methods are well-established for investigating the unsteady flame behaviors where OH^* signal is often assumed to be proportional to heat release rate e.g. [20–23]. Without access to sophisticated combined high-speed velocimetry and planar scalar imaging techniques, this approach can produce useful insights when combined with phase-

resolved PIV data despite the uncertainty discussed in Refs. [24,25]. Proper orthogonal decomposition (POD) analysis of the OH^* images were conducted to examine dominant unstable flame structures. Volume and time integrated Rayleigh indices have also been evaluated to quantify the differences in the driving and damping regions of the two flames. The mechanisms and the dynamic responses of the CH_4 and $0.9H_2/\ 0.1CH_4$ flames are described. How these insights can support the development of fuel-flexible gas turbine combustors are also discussed.

3. Experimental setup and diagnostic

A schematic of the experimental setup and specifications of the LSI are shown in Fig. 2 with details given in Ref. [19]. The quartz combustor is the one in Ref. [13] but without the exit constriction to simplify acoustics analysis. Of the five pressure taps, P1–P5, only P3 is fitted with a high-fidelity pressure transducer (Honeywell SPTMV0003PG). Previous acoustics analysis of the P1–P5 signals showed P3 to be near the anti-node of the acoustics system that includes the combustion chamber and the LSI feed tube. Conditions of the two flames are shown in Fig. 1 on their photographs. Both incite pressure oscillations at frequencies close to the 1 L mode of 324 Hz with Strouhal number of 13.6 for the CH_4 flame and 13.7 for the $0.9H_2/0.1CH_4$ flame. Despite having a higher heat release rate, p' of the CH_4 flame is 10 db lower than the $0.9H_2/0.1CH_4$ flame. Phase-resolved PIV data reported in Ref. [19] are used here to support the unsteady heat release analysis. These data were obtained by time-delay triggering at eight phases of an oscillation cycle of P3 (see Fig. 1 insert). The PIV camera had a 12×12 cm off centered field-of-view (FOV) covering the flow in the dump-plane corner. The oscillating flame structures were recorded at 4 kHz by two video cameras. A Phantom V12.1 camera of 1280×800 pixel resolution (18.3×12.2 cm FOV) captured flame light emission. For OH^*, a Phantom V7.3 camera of 800×600 pixel (14.2×10.75 cm FOV) was used with a lens coupled VideoScope International VS4-1845HS-UV intensifier fitted with an Omega narrow band pass (308 ± 10 nm) filter. Lenses for the two cameras provide approximately 12 mm depth-of-field to capture the temporal flame motions and light emissions. The two cameras were mounted on opposite sides of the combustion chamber. They were triggered and recorded simultaneous with the P3 signal for 0.58 s.

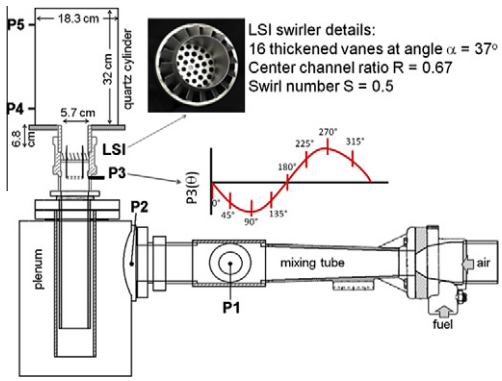

Fig. 2. The LSI and schematics of the experiment.

4. Proper orthogonal decomposition (POD) analysis

Since its introduction by Lumley [26] for studying coherent turbulent flow structures, POD has evolved into a useful tool for investigating coherent flowfield and flame structures of unsteady flames [7,23]. Here, the construction of the proper orthogonal modes (POMs) was performed by the methods of snapshots Ref. [27]. The images were considered as a collection of data with elements $\{x_i\}$, 1,2...,N, of m by n pixels belonging to a linear metric space Ω with inner product

$$\langle x, y\rangle = \int x(s)y(s)ds, \quad x, y \in \Omega \tag{1}$$

where $\langle\cdot,\cdot\rangle$ is the L_2 inner product $\sum_j\sum_j x(j,k,)y(j,k)$. The 0-th POM is the mean

$$\varphi_0 = \frac{1}{N}\sum_i^N x_i \tag{2}$$

The modes are calculated from the $N \times N$ correlation matrix K with entries

$$K_{i,j} = \langle \widetilde{x_i}, \widetilde{x_j}\rangle \tag{3}$$

where $\widetilde{x_i} = x_i - \varphi_0$ is the deviation from the mean image φ_0. The solution of the eigenvector problem

$$Kv_r = e_r v_r \tag{4}$$

gives N eigenvalues, $e_1 \geq e_2 \geq \cdots \geq e_N$. From each eigenvalue pair, the mode φ_r is constructed by linear combination of the N images,

$$\varphi_r = \sum_{i=1}^N v_{r,i}x_i \quad r = 1 \ldots .N \tag{5}$$

The projection of $\{\widetilde{x_i}\}$ into φ_r generates the series

$$a_{r,i} = \langle \widetilde{x_i}, \varphi_r\rangle \quad i = 1 \ldots N \tag{6}$$

Data reduction is achieved by taking only the first M modes, $M < N$

$$Z_{M,i} = \varphi_0 + \sum_{r=1}^M a_{r,i}\varphi_r \tag{7}$$

For consecutive images obtained at a regular sampling rate, $a_{r,i}$ can be interpreted as a time series for mode φ_r from which power spectral density (PSD) can be deduced to investigate if a dominant frequency f_r exists for the pattern represent by mode r. Other statistical analysis such as cross correlation can also be performed to infer the underlying physical processes associates with the various modes.

5. Results

In Fig. 3, representative flame light images at four phases of the oscillation cycle are compared with the phase-resolved streamtraces from PIV. Also listed are the volumetric flux, V_θ/V_0. As outlined by the streamtraces, vortex rings shed from the LSI rim dominate both flames. In the central region, spreading of the streamtraces is characteristic of a divergent flow. For the CH_4 flame, the images show a central bowl-shaped flame with its trailing edge impinging on the combustor wall and folding upstream. Intermittent flashback along the OSL can be seen by eye but there is no evidence of flame attachment. As reported in [19], the traveling ring vortices in the OSL merge with a standing ring vortex trapped below the flame impingement point. The interaction between the rolled-up flame and the trailing edge of the bowl-shaped flame appears to be the mechanism that creates flame folding.

The $0.9H_2/0.1CH_4$ flame shows very different flame structures. The attached part consists of traveling roll-up flame structures moving synchronously with the vortex centers. This explains the regular flame oscillations in this region. The central part of the flame is disk-shaped which appears to expand radially when the vortex center approaches (90°) and contract as it passes. The video suggests periodic vertical bulk flame movements, which explains flame oscillations measured on the centerline. The $0.9H_2/0.1CH_4$ flame is more compact and closer to the LSI exit than the CH_4 flame. It does not extend to the combustor wall and allows the traveling vortex to escape. This oscillating flame generates variations in V_θ/V_0 of up to +25% and −32%. The magnitude of V_θ/V_0 is significantly higher than for the CH_4 flame and the results reported in the literature for high-swirl flames.

The global behaviors of heat release oscillations in the two flames (assuming that OH^* intensity is proportional to heat release rate) are compared in Fig. 4 by the mean OH^* axial profiles obtained by integrating the intensities of the

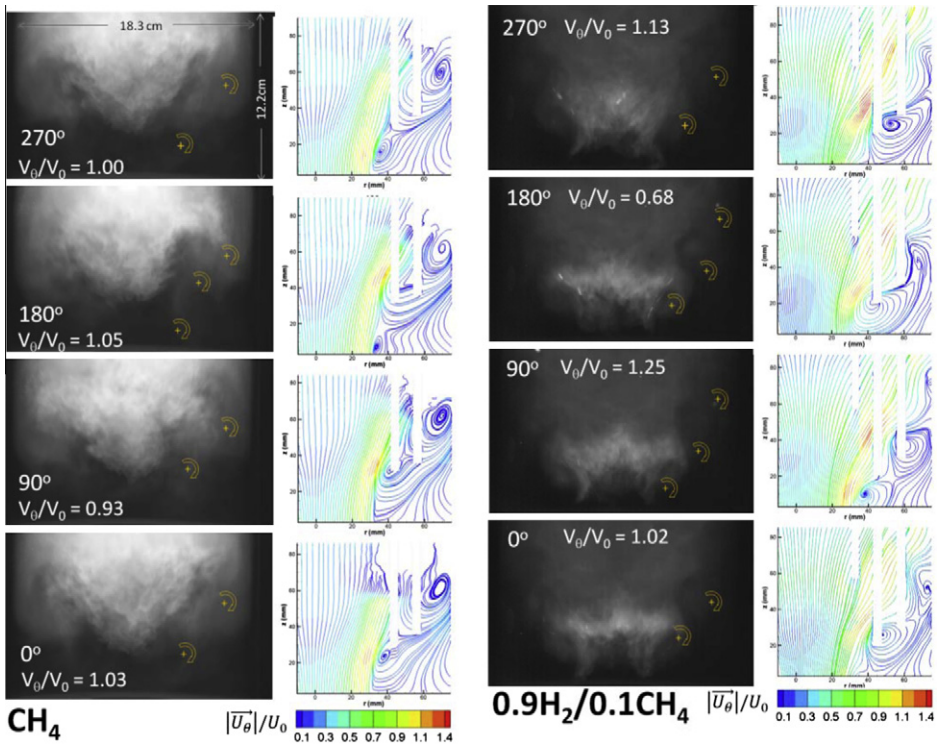

Fig. 3. Flame light images and streamtraces at four phases of the oscillation cycle. + on photos marks the vortex centers and the rotation direction. V_θ/V_0 is the normalized phase resolved volumetric flow rate and U_θ/U_0 is the normalized phase resolved velocity magnitude from Ref. [19].

horizontal pixel rows. For the CH_4 flames, cyclic variation in OH^* are found between $50 < z < 90$ mm, where the trailing edge of the bowl-flame folds back. The shape of the contours indicates temporal fluctuations with some cycle-to-cycle variations instead of cyclic shifts in the heat release location. In comparison, heat release of the $0.9H_2/0.1CH_4$ flame occurs closer to the LSI exit. Very regular temporal heat release fluctuations take place throughout the flame region of $10 < z < 65$ mm with very low cycle-to-cycle variations. At $z < 20$ mm, heat release fluctuations are consistent with the traveling roll-up flame structures. Significant variations at $30 < z < 50$ mm are generated by the oscillating central flame and the OSL flame. Oscillations above $z = 50$ mm may be explained by the cyclic contracting (thickening) and expanding (stretching) of the disk flame.

The flame structures corresponding to the heat release fluctuations are investigated by POD analysis of the OH^* data. Figure 5 compares the pressure spectra and the PSDs for the first six POD modes (POMs). For the CH_4 flame, all PSDs have a 317 Hz peak which corresponds to the dominant peak of the p' spectrum. However, lower frequencies contributions are also found. For some modes, the low frequencies have higher energy levels than the 317 Hz peak, but do not rise significantly above the characteristic $1/f$ noise spectrum floor. The p' spectrum also has a weaker peak at 490 Hz which we identified to be associated with the plenum and the premixer. This frequency is not evident in the POM data because it did not trigger any flame responses. The Eigenvalues show that there is no dominant mode because the highest energy contributed by POM1 is 4.9%. In contrast, the PSDs of the first two modes of the $0.9H_2/0.1CH_4$ flame have strong 335 Hz

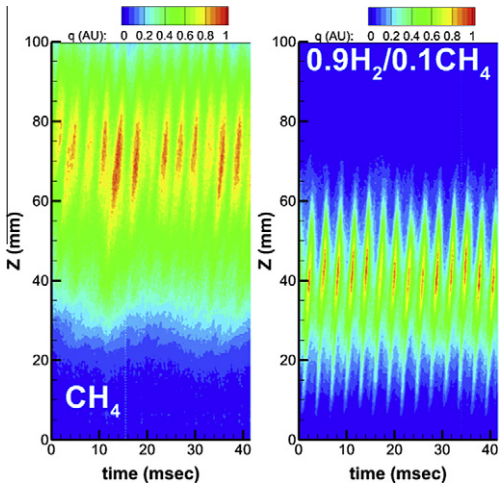

Fig. 4. Time series of axial mean OH^* profiles.

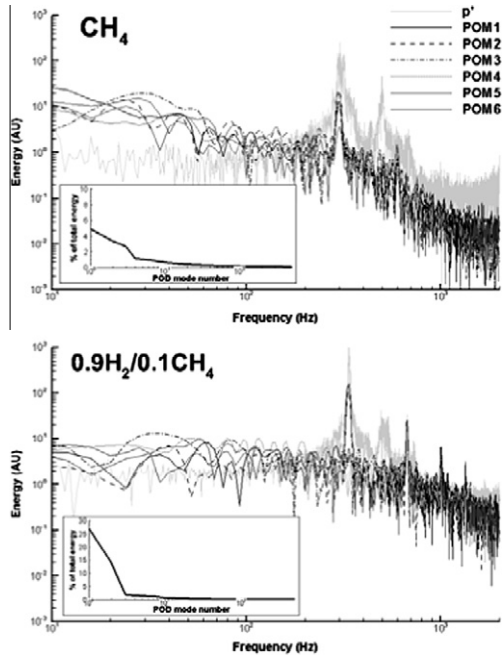

Fig. 5. Pressure spectrum and PSDs for the first six POMs. Inserts show eigenvalues e_1 to e_N of the POMs.

peaks corresponding to the p' peak. Higher harmonic peaks are also visible on the PSDs. The Eigenvalues show the first two modes are significantly higher than higher modes, showing their dominance on heat release oscillations.

The first six mode shapes are compared in Fig. 6. For CH_4, POM1 is axisymmetric and assumes the scale and shape of the lifted flame. Its f_D, 8 Hz, is likely noise because it also has a peak at 317 Hz. POM2 and 3 are also axisymmetric and of large scales. The shapes in the upper regions are consistent with the flame structures at the trailing edge of the flame. Both f_D are at the thermoacoustic frequency of 317 Hz and their peaks are higher than the POM1 peak. Cross-correlation of $a_{r,i}$ for POM2 and 3 shows them to follow an elliptical orbit having a phase difference of 90°. This means that the two modes form a pair, to indicate a convective nature of the unstable flame structures. These two modes contribute 6% of total heat release fluctuations. POM4–6 are not axisymmetric and have smaller scales. They contribute from 0.7% to 1.1% of the total energy and no pairing is found for these higher modes.

For the $0.9H_2/0.1CH_4$ flame, the dominant POM1 and 2 are axisymmetric and assume the scale and shape of large roll-up flame structures. Cross-correlation of their $a_{r,i}$ shows them to be a strongly coupled pair with phase shift at 90°. These two modes contain 40% of energy at the thermoacoustisc frequency of 335 Hz. Modes

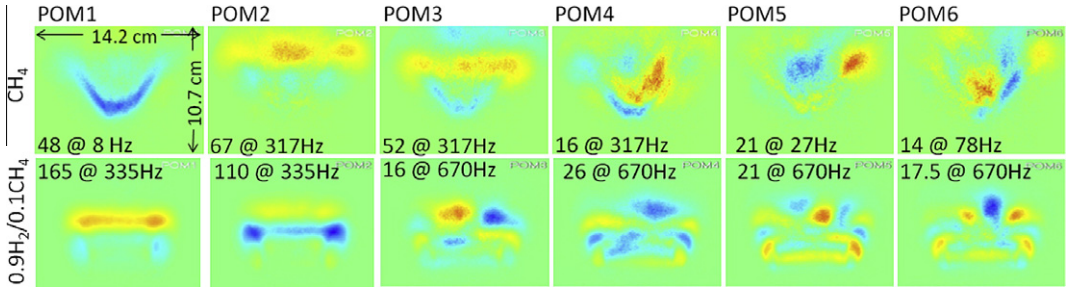

Fig. 6. Mode shapes from POD analysis with the corresponding f_D and their energy levels.

3–6 are not axisymmetric and has smaller scale features, with a much lower fraction of the energy content (1.0–1.7%) at a first harmonic frequency of 670 Hz. Cross-correlation did not show pairing of these higher modes.

The dominant POD mode shapes show that the thermoacoustically coupled heat release fluctuations in both flames are associated with the large roll-up flame structures. A thermoacoustic model of the combustor can be developed by filtering the POD results at the 1 L frequency of the combustor system and applying a Galerkin projection of the heat release on to the 1 L mode shape. This would improve the heat release model beyond the capabilities of the n–τ model previously applied to this combustion system [19].

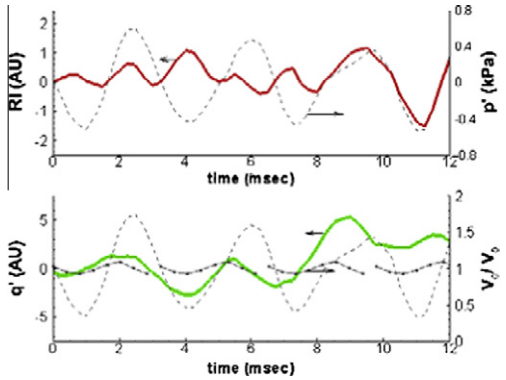

Fig. 7. Temporal variations of mean RI and q' for the CH_4 flame.

6. Rayleigh indices

The integrand of the Rayleigh integral (Eq. (8)) is often termed the Rayleigh index (RI) and is useful for identifying regions where thermoacoustic driving and damping occurs.

$$R = \int\int \mathrm{RI}(r,\theta,z,t)\,dVdt = \int\int q\prime(r,\theta,z,t)p\prime(r,\theta,z,t)\,dVdt \quad (8)$$

Here, RI was calculated using the OH^* images and longitudinal mode shape of p' (see Fig. 7 Ref. [19]). Figure 7 compares the temporal variation of the volume integrated RI, p', q', and V_θ/V_0 for the CH_4 flame. As PIV results are phased averaged, V_θ/V_0 are plotted repeatedly for each cycle. The q' trace shows irregular fluctuations that do not exhibit a strong phase relations with p'. Significant cycle-to-cycle variation is quite obvious. The V_θ/V_0 result is also cyclic. The mismatch at the end and the beginning of the cycle (i.e. the unconnected points of the trace) is most likely due to phase jitter which is an unavoidable uncertainty associated with the technique. Despite the mismatch, V_θ/V_0 appears to be in phase with q'. The corresponding RI result is cyclic but without regularity in driving (+ve) or damping (−ve). Each of the RI cycle has different features. The first cycle has weak +RI peaks at $\theta = 90^o$ and 270^o, the second has one peak, the third shows an irregular cycle.

In Fig. 8, q' in the $0.9H_2/0.1CH_4$ flame shows more regularity than in the CH_4 flame. Because q' is almost in phase with p', the RI experiences

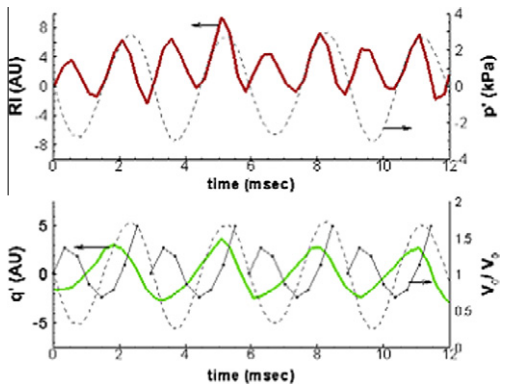

Fig. 8. Temporal variations of mean RI and q' for the $0.9H_2/0.1CH_4$ flame.

a frequency doubling and rectification compared to p' or q', and possesses nearly all positive values over a cycle. The heat release amplitude has reached a nearly steady state condition, and the RI is nearly positive at all times, damping must exist at some other location in the system, likely boundary admittance, to prevent growth without bound. Though limit cycle behavior is shown on Fig. 8, we also observed that heat release and flow transients also caused phase jitter such that as time progresses, the heat release locks in and out with the acoustics mode. As discussed earlier, V_θ/V_0 in the $0.9H_2/0.1CH_4$ flame is much higher than in the CH_4 flame which can be explained by the significantly higher acoustic driving shown by the RI profile. Additionally, the V_θ/V_0 is 90^0 out-of-phase with p', and the end-of-cycle mismatch is large. It is difficult to assign mismatch of this magnitude to phase jitter. Therefore, it may be necessary to repeat the measurements by shifting the trigger start by 180^0 to resolve the flowfield structures at the point of maximum q'.

The time and radial integrated RI for the CH_4 flame are shown in Fig. 9. The RI maps correspond to instances of driving. The one for $q' < 0$ and $p' < 0$ shows regions of driving at $z >$ 80 mm. The regions of both driving and damping below are consistent with random turbulent flame fluctuations. The net result is an axial RI distribution (along the broken line on the contour plot) that shows a +ve RI zone centered at $z =$ 80 mm. The RI map for $q' > 0$ and $p' > 0$ shows a driving region at $z > 60$ mm. The axial RI distribution shows this to be an instance where the driving region occurs further upstream. Otherwise, the driving region of the other cycles are mostly near $z = 80$ mm where the roll-up flame structure meet the trailing flame generating heat release fluctuations. Although the OH^* images do not show the mechanism clearly, these results

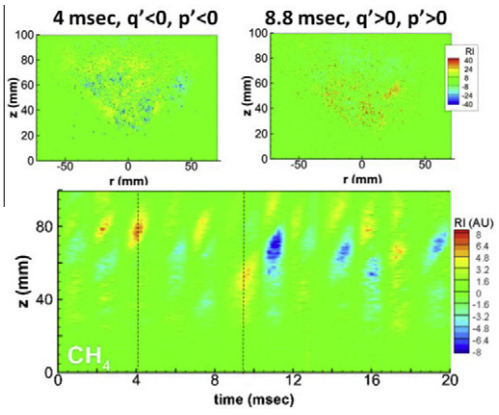

Fig. 9. RI maps (top) and temporal variations of mean axial RI (bottom) for the CH_4 flame.

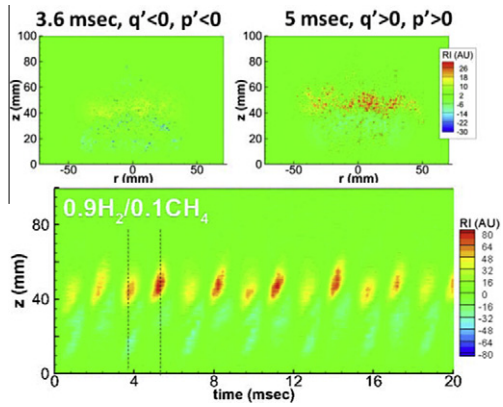

Fig. 10. RI maps (top) and temporal variations of mean axial RI (bottom) for the $0.9H_2/0.1CH_4$ flame.

are consistent with the notion of flame folding by the rolled up flame structures associated with the standing vortex.

The 2D RI maps and axial profiles for the $0.9H_2/0.1CH_4$ flame are shown in Fig. 10. For $q' < 0$ and $p' < 0$, the 2D RI map shows horizontal layers of driving and damping consistent with the disk flame shape seen in Fig. 3 at 90^o. The corresponding axial RI distribution has a broad driving region centered on $z = 45$ mm. For $q' > 0$ and $p' > 0$ diving is much stronger by a narrow band of +ve RI at $z = 40$ mm corresponding to the top of the thickened disk flame shown in Fig. 3 at $\theta = 270^o$. The video shows this instance to be at the point just after the roll-up flame structures in the OSL merge with the flat flame. The consequence is a high concentration of 'flame surfaces[1]' that generates stronger local driving than at $q' < 0$ and $p' < 0$ (see RI(z, t) contours below). Additionally, the shape of the RI(z, t) contours at $q' > 0$ and p' 0 suggests convection of the driving region downstream. These results clearly show that flame folding at the edge of the central flat flame shape is the driving mechanism of the $0.9H_2/0.1CH_4$ flame instabilities. Therefore, flame oscillations measured previously on the centerline are most likely a consequence of the V_θ/V_0 fluctuation. This mechanism is quite unlike the finding of Bellows et al [21] where the periodic detachment and reattachment of the high-swirl flame from the center body contributes to flame surface area generation and destruction. To continue this study, we plan to apply the diagnostics and analysis to the other

[1] Flame surface density of high-hydrogen content fuels is not a good surrogate for heat release density because of non-uniform burning due to thermal/diffusive effects [28].

acoustically coupled and uncoupled flames reported by Therkelsen et al. [19], and examine the cause and consequence of heat release and pressure oscillations.

7. Conclusion

The fuel effects on the dynamic response of LSI flame to self-excited oscillations has been studied by high-speed flame and OH^* imaging of two thermoacoustically coupled flames burning CH_4 (113 kW) and a fuel blend of $0.9H_2/0.1CH_4$ (74 kW). The flames have different shapes but generate pressure and flame oscillations near the 1 L mode frequency of the system. The CH_4 flame is lifted and the $0.9H_2/0.1CH_4$ attaches to the LSI rim. PIV shows flowfields of both flames are dominated by traveling ring vortices shed from the rim. The vortices of the CH_4 burn intermittently and those in the $0.9H_2/0.1CH_4$ burn consistently.

Analyses of the OH^* results by proper orthogonal decomposition show different flame structures are responsible for generating flame oscillations. Fluctuations of the CH_4 flame are generated by a broad range of structures. The one that oscillates at the acoustics frequency is a rolled-up flame near the standing ring vortex below the trailing edge of the lifted flame. Flame oscillations in the $0.9H_2/0.1CH_4$ flame are dominated by the traveling rolled-up flame merging from the LSI rim. As a result, all the flame structures oscillate at the acoustic frequency or the higher harmonics.

Analyses of the Rayleigh index show more regular and stronger driving in the $0.9H_2/0.1CH_4$ flame than in the CH_4 flame. This is due to the merging of the central flat region of the $0.9H_2/0.1CH_4$ flame with the rolled-up structures in the OSL resulting in a narrow region with high heat release density. Rapid heat release increase/decrease due to variations in the flow of the reactants is also responsible for the non-linear effects. Driving in the CH_4 is much weaker because the flame folding mechanism does not seem to be regular.

Flame attachment due to high reactivity of H_2 has a significant effect on how the LSI responds to self-excited flame oscillations. Significantly higher acoustic driving is generated by the compact shape of the flame and its flame folding dynamics. To reduce the likelihood of this type of combustion instability in a fuel flexible LSI gas turbine combustor mitigation of flame attachment and/or deferring the formation of the outer shear layer is needed. This effectiveness of this approach has been demonstrated recently at atmospheric and simulated gas turbine conditions [29,30] where LSIs fitted with divergent quarls are shown to reduce combustion oscillations.

Acknowledgement

This work was supported by the Assistant Secretary for Fossil Energy, Advanced Turbines Program, of the U.S. Department of Energy under Contract No. DE-AC02-05CH11231.

References

[1] D.T. Harje, F.H. Reardon, *Liquid Propellant Rocket Combustion Instability*, NASA SP 194, 1972.
[2] F. Culick, *Unsteady Motions in Combustion Chambers for Propulsion Systems*, RTO AGARDograph, AG-AVT-039, NATO, 2006.
[3] T. Lieuwen, V. Yang, *Combustion Instabilities in Gas Turbine Engines*, AIAA Progress in Astronautics and Aeronautics Vol 210 2005.
[4] S.K. Thumuluru, T. Lieuwen, *Proc. Combust. Inst.* 32 (2) (2009) 2893–2900.
[5] H.J. Lee, K.T. Kim, J.G. Lee, B.D. Quay D.A. Santavicca, GT2009-6009, ASME Turbo Expo Orlando, Florida, 2009.
[6] M. Stöhr, R. Sadanandan, W. Meier, *Proc. Combust. Inst.* 32 (2) (2009) 2925–2932.
[7] A.M. Steinberg, I. Boxx, M. Stöhr, C.D. Carter, W. Meier, *Combust. Flame* 157 (12) (2010) 2250–2266.
[8] T. Lieuwen, V. McDonell, E. Petersen, D. Santavicca, *J. Eng. Gas Turbines Power* 130 (1) (2008) 011506.
[9] K.T. Kim, J.G. Lee, H.J. Lee, B.D. Quay, D.A. Santavicca, *J. Eng. Gas Turbines Power* 132 (4) (2010) 041502.
[10] R.K. Cheng, D.T. Yegian, M.M. Miyasato, et al., *Proc. Combust. Inst.* 28 (2000) 1305–1313.
[11] M.R. Johnson, D. Littlejohn, W.A. Nazeer, K.O. Smith, R.K. Cheng, *Proc. Combust. Inst.* 30 (2005) 2867–2874.
[12] D. Littlejohn, R.K. Cheng, D.R. Noble, T. Lieuwen, *J. Eng. Gas Turbine Power* 132 (1) (2010) 011502–011510.
[13] R.K. Cheng, D. Littlejohn, P. Strakey, T. Sidwell, *Proc. Combust. Inst.* 32 (2009) 3001–3009.
[14] R.K. Cheng, D. Littlejohn, W.A. Nazeer, K.O. Smith, *J. Eng. Gas Turbines Power* 130 (2) (2008) 21501–21511.
[15] D.M. Kang, F.E.C. Culick, A. Ratner, *Combust. Flame* 151 (3) (2007) 412–425.
[16] Y. Huang, A. Ratner, *J. Propul. Power* 25 (2) (2009) 365–373.
[17] S. Tachibana, J. Yamashita, L. Zimmer, K. Suzuki, A.K. Hayashi, *Proc. Combust. Inst.* 32 (2) (2009) 1795–1802.
[18] I. Yilmaz, A. Ratner, M. Ilbas, Y. Huang, *Int. J. Hydrogen Energy* 35 (1) (2010) 329–336.
[19] P.L. Therkelsen, J.E. Portillo, D. Littlejohn, S.M. Martin, R.K. Cheng, *Combust. Flame*, in press.
[20] R. Balachandran, B.O. Ayoola, C.F. Kaminski, A.P. Dowling, E. Mastorakos, *Combust. Flame* 143 (1–2) (2005) 37–55.
[21] B.D. Bellows, M.K. Bobba, A. Forte, J.M. Seitzman, T. Lieuwen, *Proc. Combust. Inst.* 31 (2) (2007) 3181–3188.

[22] K.T. Kim, J.G. Lee, B.D. Quay, D.A. Santavicca, *Combust. Flame* 157 (9) (2010) 1718–1730.
[23] M. Stöhr, R. Sadanandan, W. Meier, *Exp. Fluids* 51 (4) (2011) 1153–1167.
[24] V. Nori, J. Seitzman, AIAA 2008-0953, 46th Aerospace Sciences Meeting, AIAA, Reno, NV, 2008.
[25] V.N. Nori, J.M. Seitzman, *Proc. Combust. Inst.* 32 (1) (2009) 895–903.
[26] J.L. Lumley, *The Structure of Inhomogeneous Turbulence*, Nauka, Moscow, 1967, pp. 166–178.
[27] P. Holmes, J.L. Lumley, G. Berkooz, *Turbulence Coherent Structures Dynamical Systems and Symmetry*, Cambridge University Press, Cambridge., 1996.
[28] J.B. Bell, R.K. Cheng, M.S. Day, I.G. Shepherd, *Proc. Combust. Inst.* 31 (1) (2007) 1309–1317.
[29] P.L. Therkelsen, D. Littlejohn, R.K. Cheng, J.E. Portillo, S.M. Martin, GT2010-23498, ASME Turbo Expo 2010, Glasgow, United Kingdom, 2010.
[30] D. Beerer, V.G. McDonnell, P.L. Therkelsen, R.K. Cheng, GT2012-68216, ASME Turbo Expo 2012, Copenhagen, Denmark, 2012.